Acta Crystallographica Section B
Structural Science
ISSN 0108-7681

Structure analysis of titanate nanorods by automated electron diffraction tomography

Iryna Andrusenko,[a] Enrico Mugnaioli,[a] Tatiana E. Gorelik,[a] Dominik Koll,[b] Martin Panthöfer,[b] Wolfgang Tremel[b] and Ute Kolb[a]*

[a]Institut für Physikalische Chemie der Johannes Gutenberg-Universität, Welderweg 11, D-55099 Mainz, Germany, and [b]Institut für Anorganische Chemie und Analytische Chemie der Johannes Gutenberg-Universität, Duesbergweg 10-14, D-55099 Mainz, Germany

Correspondence e-mail: kolb@uni-mainz.de

Received 21 February 2011
Accepted 18 April 2011

A hitherto unknown phase of sodium titanate, $NaTi_3O_6(OH)\cdot 2H_2O$, was identified as the intermediate species in the synthesis of TiO_2 nanorods. This new phase, prepared as nanorods, was investigated by electron diffraction, X-ray powder diffraction, thermogravimetric analysis and high-resolution transmission electron microscopy. The structure was determined *ab initio* using electron diffraction data collected by the recently developed automated diffraction tomography technique. $NaTi_3O_6(OH)\cdot 2H_2O$ crystallizes in the monoclinic space group $C2/m$. Corrugated layers of corner- and edge-sharing distorted TiO_6 octahedra are intercalated with Na^+ and water of crystallization. The nanorods are typically affected by pervasive defects, such as mutual layer shifts, that produce diffraction streaks along c*. In addition, edge dislocations were observed in HRTEM images.

1. Introduction

In 1991 O'Regan and Graetzel published an article on the use of a colloidal TiO_2 film as electrode material for a very efficient dye-sensitized solar cell (DSSC; O'Regan & Graetzel, 1991), demonstrating the usefulness of TiO_2 nanoparticles in technological applications. Ever since TiO_2 nanoparticles have been synthesized in various sizes and morphologies (Chen & Mao, 2007) and have been utilized in a multitude of applications, such as photocatalysis (Kim *et al.*, 2009; Strandwitz *et al.*, 2010), dye-sensitized solar cells (Graetzel, 2001), gas sensors (Varghese *et al.*, 2003), hydrogen storage (Lim *et al.*, 2005) or electrochromic devices (Bach *et al.*, 2002).

In order to obtain highly efficient DSSCs two counteracting requirements have to be met. First a large number of dye/semiconductor interfaces is needed to ensure a high photocurrent (*i.e.* high surface area), and at the same time a high transport rate of electrons towards the front electrode is necessary (*i.e.* few grain boundaries). By using TiO_2 nanorods as an additive to the commonly used nanoparticular TiO_2 semiconductor, these demands can be met.

Sodium titanate nanorods represent an important intermediate product in the synthesis of TiO_2 nanorods. They can be obtained from any TiO_2-based precursor by hydrothermal treatment in a highly concentrated NaOH solution (Kasuga *et al.*, 1998). The hydrothermal synthesis of sodium titanate nanorods yields microcrystals with a length of up to 10 µm, which are difficult to produce using other synthetic routes. Still, the reaction product is very polydisperse. These sodium titanate precursors can be converted to TiO_2 *via* an acidic treatment, followed by calcination.

Despite the importance of sodium titanate nanorods as a precursor for long TiO_2 nanorods, little effort has been made to investigate the crystal structure of these nanostructures.

The widely accepted model which was proposed by Chen *et al.* (2002) claims that $Na_2Ti_3O_7$ is formed under the reaction conditions mentioned above. Nevertheless, often low-quality X-ray powder diffraction data are presented, which renders a real phase determination very difficult (Kolen'ko *et al.*, 2006). Well resolved X-ray powder diffraction patterns, on the other hand, do not match the line pattern of $Na_2Ti_3O_7$ (Peng *et al.*, 2008). Recent results by Peng *et al.* (2008) point towards a different composition, yet a detailed structural analysis is missing. Knowing the crystal structure of this sodium titanate might give insight into the formation mechanism of the long nanorods and may aid the synthesis of a more defined reaction product.

In this paper we report the structure of $NaTi_3O_6(OH)\cdot 2H_2O$ nanorods as determined using electron diffraction data collected by automated diffraction tomography (ADT). ADT, a new strategy for electron diffraction data collection and processing, is able to deliver in an automated way rich and quasi-kinematical electron diffraction data sets from single nanocrystals (for a detailed description of ADT see Kolb *et al.*, 2007, 2008, 2009; Mugnaioli *et al.*, 2009). In recent years ADT has been used successfully in a number of *ab initio* structure solutions, even for complicated and beam-sensitive samples (Birkel *et al.*, 2010; Denysenko *et al.*, 2011; Kolb *et al.*, 2010; Rozhdestvenskaya *et al.*, 2010).

2. Experimental

2.1. Synthesis

The synthesis was carried out using a MARS XPress microwave digestion system (CEM Corporation). The procedure was derived from the work published by Kasuga *et al.* (1998) and was modified to be suitable for the reaction system.

In a typical synthesis 500 mg of titania powder (TiO_2-P25, Degussa) were mixed with 50 ml of a 10 *M* NaOH solution (made from NaOH pellets, 98.5%, p.A., Acros Organics) by vigorous magnetic stirring for 15 min in a 100 ml Teflon liner. Afterwards the vessel was sealed and subjected to hydrothermal treatment in a microwave furnace. The reaction mixture was heated over 10 min until an internal pressure of 20 bar was reached. This pressure was kept constant for 2 h. Due to the technical limitations of the microwave reaction system a direct measurement of the reaction temperature was not possible under these reaction conditions. The maximum energy output was set to 800 W. When the reaction was finished, the mixture was allowed to cool down radiatively for 30 min.

After the synthesis the supernatant NaOH solution was removed by centrifugation (9000 rpm, 10 min) and the samples were washed repeatedly with methanol (99.8%, p.A., J. T. Baker) until a neutral reaction of the supernatant solution was reached. Finally, the samples were dried in a vacuum overnight.

2.2. TEM and ADT

For TEM and Automated Diffraction Tomography (ADT) investigations the samples were dispersed in ethanol using an ultrasonic bath. Afterwards they were sprayed on carbon-coated copper and gold grids. For high-resolution TEM investigations the material was embedded in epoxy resin and sliced by microtome. The cuts were then placed on a carbon coated copper grid; the resin was removed with chloroform.

TEM measurements were carried out with a FEI TECNAI F30 S-TWIN transmission electron microscope working at 300 kV. TEM images and diffraction patterns were acquired with a CCD camera (14-bit GATAN 794MSC). Scanning transmission electron microscopy (STEM) images were acquired by a FISCHIONE high angular annular dark field (HAADF) detector. Elemental analysis was done by energy-dispersive X-ray (EDX) spectroscopy and quantified within Emispec *ESVision* software. For a quantitative EDX analysis the sample was deposited on an Au grid.

In order to perform structure analysis, three-dimensional electron diffraction data were collected using an ADT module (Kolb *et al.*, 2007). Within the module, the crystal position is tracked in microprobe scanning transmission electron microscopy (STEM) mode and nano electron diffraction patterns are collected every 1° tilt inside the possible tilt range of the microscope goniometer. A condenser aperture of 10 µm was used in order to produce a semi-parallel beam of 50 nm in diameter on the sample. For high tilt experiments a FISCHIONE tomography holder was used. In order to improve reflection intensity integration, ADT was coupled with electron beam precession (precession electron diffraction, PED), performed using a NanoMEGAS DigiStar unit (Vincent & Midgley, 1994). The precession angle was kept at 1.2°. The three-dimensional electron diffraction data were processed using an ADT three-dimensional (Schömer *et al.*, 2009) software package coupled with self-developed Matlab scripts (Kolb *et al.*, 2008, 2009; Mugnaioli *et al.*, 2009).

2.3. X-ray diffraction

X-ray powder diffraction data were collected using a Bruker-AXS D8-Discover diffractometer equipped with a HiStar detector in reflection geometry using graphite-monochromated Cu $K\alpha$ radiation. Samples were glued on top of glass and (111) silicon substrates using a VP/VA copolymer (vinylpyrrolidone/vinylacetate). Full-pattern profile fits, Pawley fits, Rietveld refinements and attempts at structure solution were performed using *TOPAS-Academic* (Coelho, 2007*a*), applying the fundamental parameter approach for reflection profiles (Cheary & Coelho, 1992).

2.4. Thermogravimetry

Thermogravimetry (TG) was performed using a NETZSCH STA 429 Thermal analyser. Roughly 50 mg of the sample was placed in a ceramic sample holder, which was covered by a ceramic cap. Gases evolving upon heating the sample were released through a hole in the ceramic cap. Data evaluation was performed with the NETZSCH *Proteus* thermal analysis

software (NETZSCH, 2004). The sample was heated from room temperature to 1373 K at a heating rate of 1 K min^{-1}.

3. Results

3.1. TEM overview

Dark-field scanning transmission electron microscopy (STEM) images show that the sample mainly consists of rods of different sizes (Fig. 1*a*). The rod diameters range from 50 to 1000 nm, while rod lengths can reach several microns. The rod edges are typically sharp, ending with flat and sharp tips. Some of the rods show a regular rectangular shape, while others are bent or consist of bundles of smaller rods (Figs. 1*b* and *c*). Beside the rods, small particles of size 20–30 nm are present in the sample. (Fig. 1*d*).

3.2. EDX

EDX spectroscopy on the rods reveals the presence of O, Na and Ti. A quantification of the Na content is problematic due to line overlap with Cu (Na K-series of 1040.98–1071.1 eV and Cu L-series of 929.7–949.8 eV), therefore, for the quantitative analysis the sample was prepared on Au TEM grids. The quantification of the Na:Ti ratio, based on respective K-lines, is close to 1:2 and is almost constant for small and large rods.

EDX analysis of the small particles surrounding the rods reveals only the presence of Na and O. The quantification of the Na:O ratio in the particles was not possible due to the weak signal from the particles. It is likely that these nanoparticles are $NaHCO_3$ or Na_2CO_3, which are formed by the uptake of CO_2 into the caustic solution from ambient air. These impurities cannot be completely removed by washing with methanol due to their low solubility in methanol (Ellingboe & Runnels, 1966). Washing the reaction product with water was avoided due to the risk of partial ion exchange of sodium by hydronium ions.

According to the proposed structure based on electron diffraction, $NaTi_3O_6(OH)\cdot 2H_2O$, the Na:Ti ratio should be 1:3. The presence of residual NaOH nanoparticles in the sample may partially explain the actual ratio of 1:2. Other authors observed an unexpectedly high amount of Na for similar nanorods and correlated it with the presence of residual Na^+ bound to the rod surface (Nagase *et al.*, 1999; Meng *et al.*, 2004). On the other hand, the presence of additional Na^+ cations between the layers cannot be excluded and may be correlated with the pervasive disorder responsible for the diffuse scattering observed in ADT three-dimensional reconstructed reciprocal space.

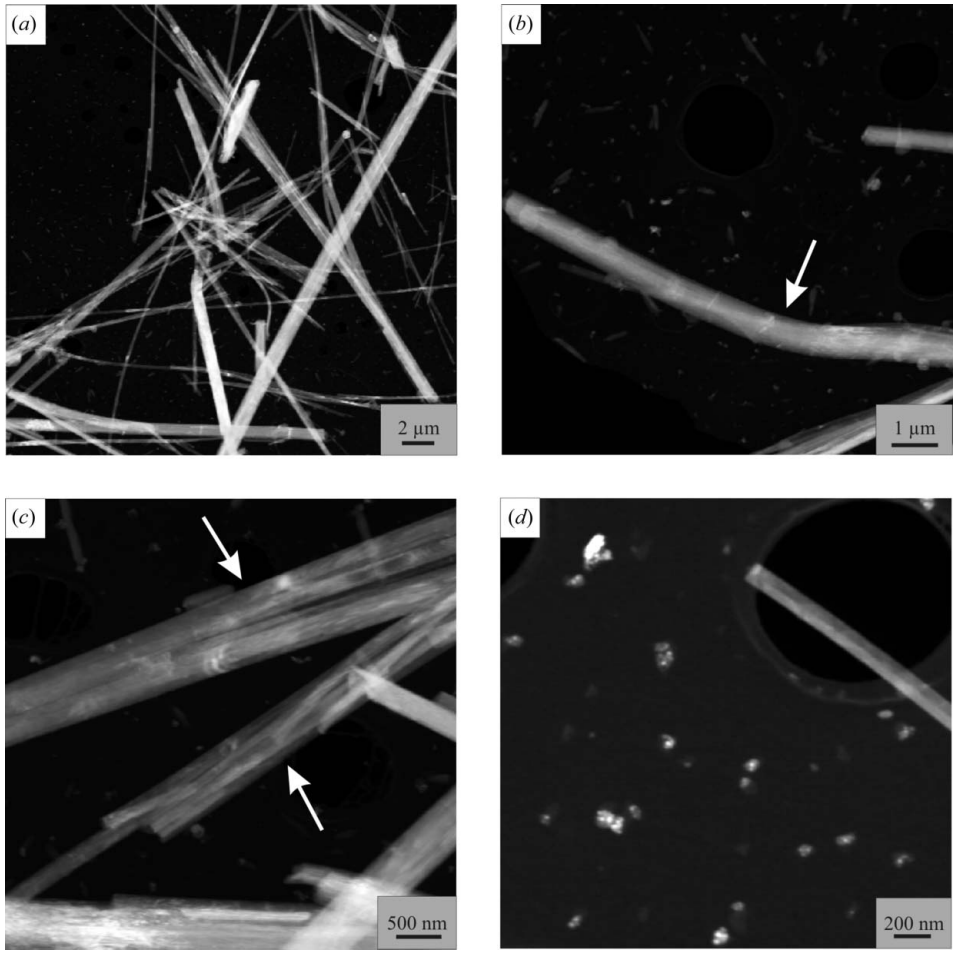

Figure 1
Low magnification STEM images of the sample: (*a*) Overview of sodium titanate nanorods; (*b*) bent nanorod; (*c*) rods consisting of bundles; (*d*) small 'NaO' particles next to a sodium titanate rod.

3.3. Thermogravimetry

Thermogravimetric (TG) measurements show three stages of weight loss in the sample (Fig. 2). From $\sim$423 to $\sim$573 K the weight decreases by 7% from its initial value. According to Peng *et al.* (2008), who investigated a sodium titanate synthesized under similar reaction conditions, this can be attributed to both the decomposition of monodentate carbonates (*e.g.* $NaHCO_3$) and an initial release of water, which is due to the loss of water of crystallization and the condensation of titanoyl groups on the surface of the nanorods. The weight loss in the region between 573 and 873 K arises from a continued slow release of water from the nanorods (Peng *et al.*, 2008). After this stage, 91.5% of the initial weight remains. Another one-step

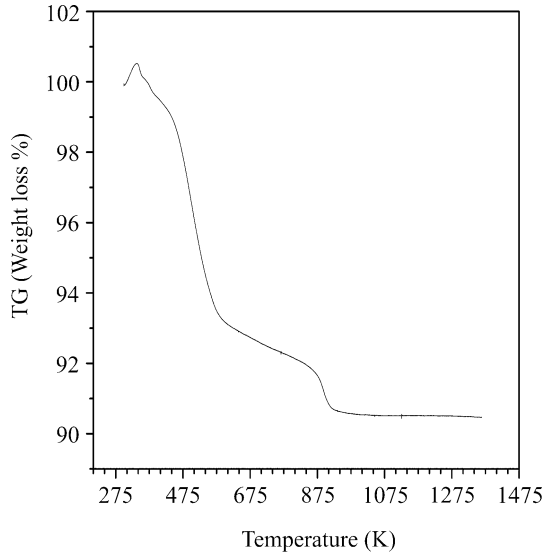

Figure 2
TG curve of sodium titanate nanorods.

weight loss occurs between 873 and 923 K. In this last step multidentate carbonates (*e.g.* Na_2CO_3) decompose and the release of water has stopped (Peng *et al.*, 2008). At higher temperatures the sample does not undergo any further change of weight. In total, 90.5% of the initial weight remains at the end of the experiment.

The TG results obtained here are in full agreement with the literature (Peng *et al.*, 2008). Nevertheless, the observed weight loss is less than expected based on the composition $NaTi_3O_6(OH)\cdot 2H_2O$. The contamination with carbonates (which may also be hydrated) mentioned above explains this difference, because NaOH or Na_2O remain in the sample after decomposition of $NaHCO_3$ and Na_2CO_3, respectively. These compounds do not further decompose under the applied sintering conditions (Weast, 1987–1988).

3.4. ADT structure analysis

Automated diffraction tomography (ADT; Kolb *et al.*, 2007, 2008) data sets were collected from six different rods of different dimensions. Tilt series were collected in steps of 1° within a total tilt range up to 120°. For all acquisitions, the reconstructed three-dimensional reciprocal volumes show more or less pronounced diffuse scattering intensities (Figs. 3*a* and *b*) visible as streaks exclusively along one crystallographic direction associated with disorder effects (Welberry, 2004).

The two tilt series exhibiting the weakest diffuse scattering contribution were selected for subsequent cell parameter determination and reflection intensity integration (Figs. 3*c* and *d*). From the selected acquisitions, a C-centred monoclinic cell with the parameters a = 21.53 (8), b = 3.79 (2), c = 11.92 (8) Å, β = 136.3 (5)°, V = 672 (17) Å^3 was determined. Systematic extinctions due to C-centring were clearly identified in all reconstructed volumes. No further extinction was identified. Therefore, three space groups were taken into consideration for the structure solution: *C*2, *Cm* and *C*2/*m*.

Table 1
Experimental parameters of the two data sets used for structure solution of $NaTi_3O_6(OH)\cdot 2H_2O$.

The tilt range of the second acquisition was limited by overlapping of the surrounding rods.

Data set	(I)	(II)
Tilt range (°)	−60/+60	−45/+40
Total reflections	1749	1133
Independent reflections	628	436
Resolution (Å)	0.8	0.8
Reflection coverage (%)	79	58
R_{sym}	0.117	0.147
Overall U (Å^2)	0.025	0.032
R (*SIR*2008 solution)	0.358	0.344

Table 2
Experimental details.

Crystal data	
Chemical formula	$NaTi_3O_6(OH)\cdot 2H_2O$
M_r	130.86
Crystal system, space group	Monoclinic, *C*2/*m*
Temperature (K)	295
a, b, c (Å)	21.53 (8), 3.79 (2), 11.92 (8)
β (°)	136.3 (5)
V (Å^3)	672 (17)
Z	8
Radiation type	Electron, λ = 0.0197 Å
μ (mm^{-1})	N/A
Crystal size (μm)	1.0 × 0.05 × 0.05
Data collection	
Diffractometer	FEI TECNAI F-30 S-TWIN TEM with automated diffraction topography (ADT) and precession electron diffraction (PED) modules
Absorption correction	None
R_{int}	0.158
Refinement	
$R[F^2 > 2\sigma(F^2)]$, $wR(F^2)$, S	0.267, 0.592, 3.73
No. of reflections	628
No. of parameters	40
No. of restraints	0
Maximum shift/su	0.863
$\Delta\rho_{max}$, $\Delta\rho_{min}$ (e Å^{-3})	0.73, −0.51

Computer programs used: *SIR*2008 (Burla *et al.*, 2007), *SHELXL*97 (Sheldrick, 2008).

The two data sets used for reflection intensity integration were collected coupling ADT with precession electron diffraction (PED). The most important parameters of the two data sets are listed in Table 1. The structure solution was performed *ab initio* by direct methods as implemented in *SIR*2008 (Burla *et al.*, 2007). A fully kinematic approach was used (I proportional to F^2). No correction was applied to the data.

For the first data set the structure solutions performed in space groups *C*2 and *Cm* showed a clearly recognizable inversion centre and were very similar to that performed in *C*2/*m*. Therefore, *C*2/*m* was chosen as the correct space group and the corresponding solution was used for further refinement.

The structure solution from the second data set basically delivered the same structural model. Imposing the space

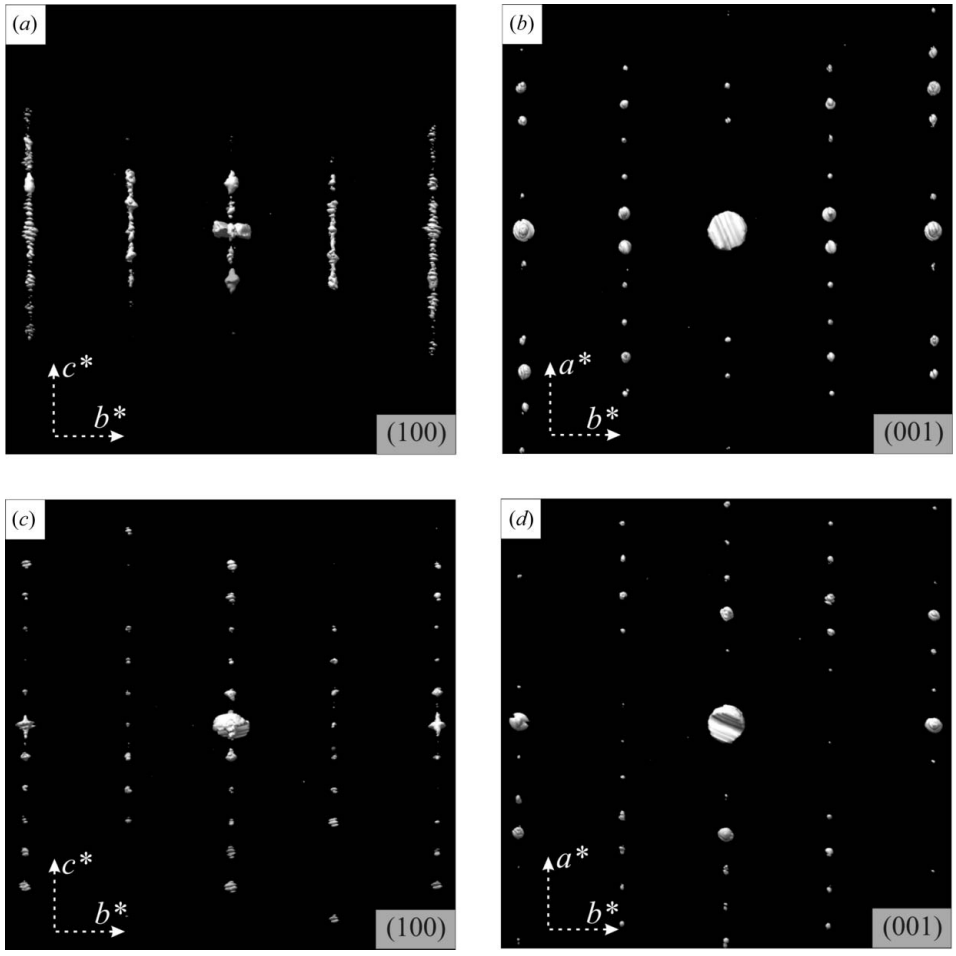

Figure 3
Projection of three-dimensional reconstructed reciprocal space from ADT data: (*a*) and (*b*) (100) and (001) projections of a strongly disordered data set; (*c*) and (*d*) (100) and (001) projections of the almost ordered data set used for structure solution. The three-dimensional reciprocal space was visualized using *UCSF Chimera* (Pettersen *et al.*, 2004). The threshold for visualization was chosen in order to emphasize the difference between the two datasets. In (100) projections the streaks along **c*** are evident for the first data set. In (001) projections no diffuse scattering is observed and the systematic extinctions due to the C-centring are well resolved.

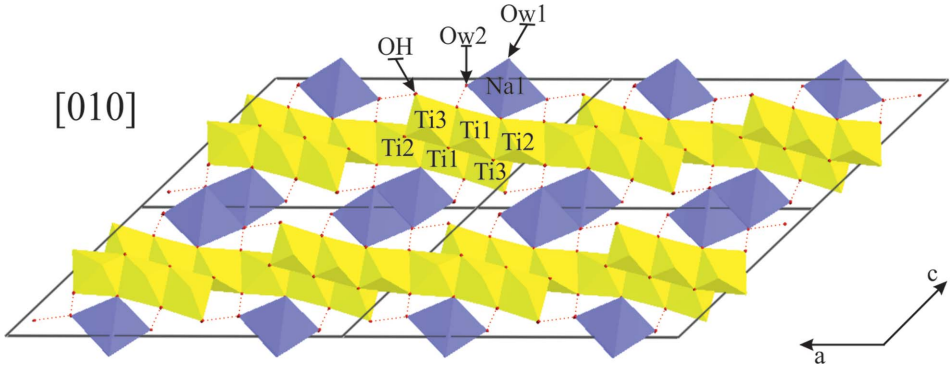

Figure 4
Final model of sodium titanate $NaTi_3O_6(OH)\cdot 2H_2O$ structure (view in [010]). H atoms omitted for the sake of clarity. $\{NaO_6\}$ octahedra are viewed edge-on. Hydrogen bonds are drawn as dotted lines.

group *C*2/*m*, the solution obtained was very similar to that obtained with the first data set, confirming the structure model.

All maxima in the electron density distribution of the obtained structure model are located on a mirror plane (y = 0.0 or 0.5). The structure consists of groups of corrugated layers of corner- and edge-sharing TiO_n polyhedra arranged parallel to the (001) plane. The three strongest maxima detected in the centres of the octahedra were assigned to the Ti atoms. The remaining weaker maxima were assigned to O, Na and water molecules of crystallization.

The model was refined against electron diffraction data sets using *SHELXL*97 (Sheldrick, 2008), without imposing any geometrical restraints (Fig. 4). The refinement was stable with a final $R1$ = 0.267. The assignment of OH^- and the two water molecules were performed based on the interatomic distances observed, thermogravimetric results and crystal chemistry considerations. The resulting composition is therefore $NaTi_3O_6(OH)\cdot 2H_2O$. Experimental details are given in Table 2.

In order to estimate the possibility of forming hydrogen bonds, H atoms were added assuming that H(water) points to the closest and the least coordinated oxygen of the $\{Ti_3O_6(OH)\}^-$ layers (*OW*1···O5 2.39 Å and *OW*2···O2 2.45 Å). The H atom of the hydroxyl group, positioned on the mirror plane in the special position 4*i*, was assumed to point toward the water (*OW*1···OH 2.36 Å) that lies on the same plane.

3.5. X-ray powder diffraction

Despite the similarities with the reported data (Peng *et al.*, 2008) the X-ray powder diffraction patterns of the samples do not fit any crystalline phase listed in the PDF-2 database (ICDD, 2004) or a plausible mixture. Owing to substantial reflection profile broadening, independent indexing of the pattern was not successful. Pawley fits based on the lattice parameters derived

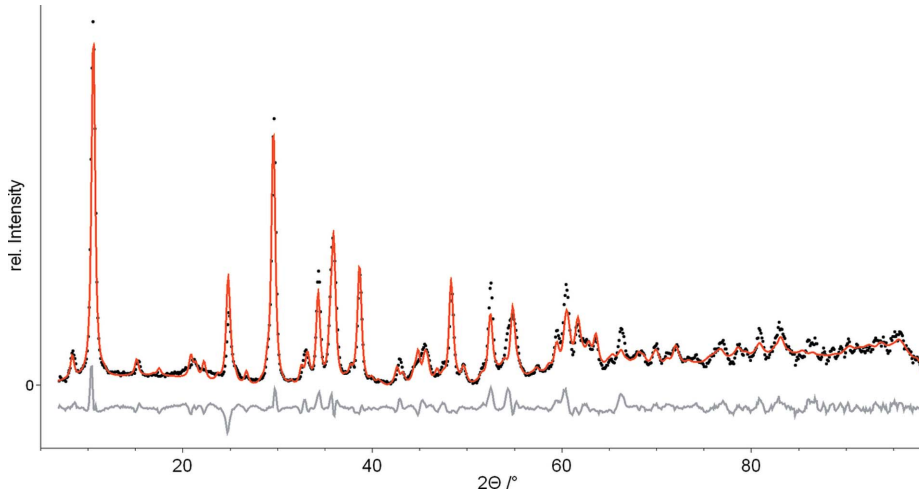

Figure 5
Rietveld fit of $NaTi_3O_6(OH)\cdot 2H_2O$. Black dots: experimental data; red line: fit; grey line: difference. This figure is in colour in the electronic version of this paper.

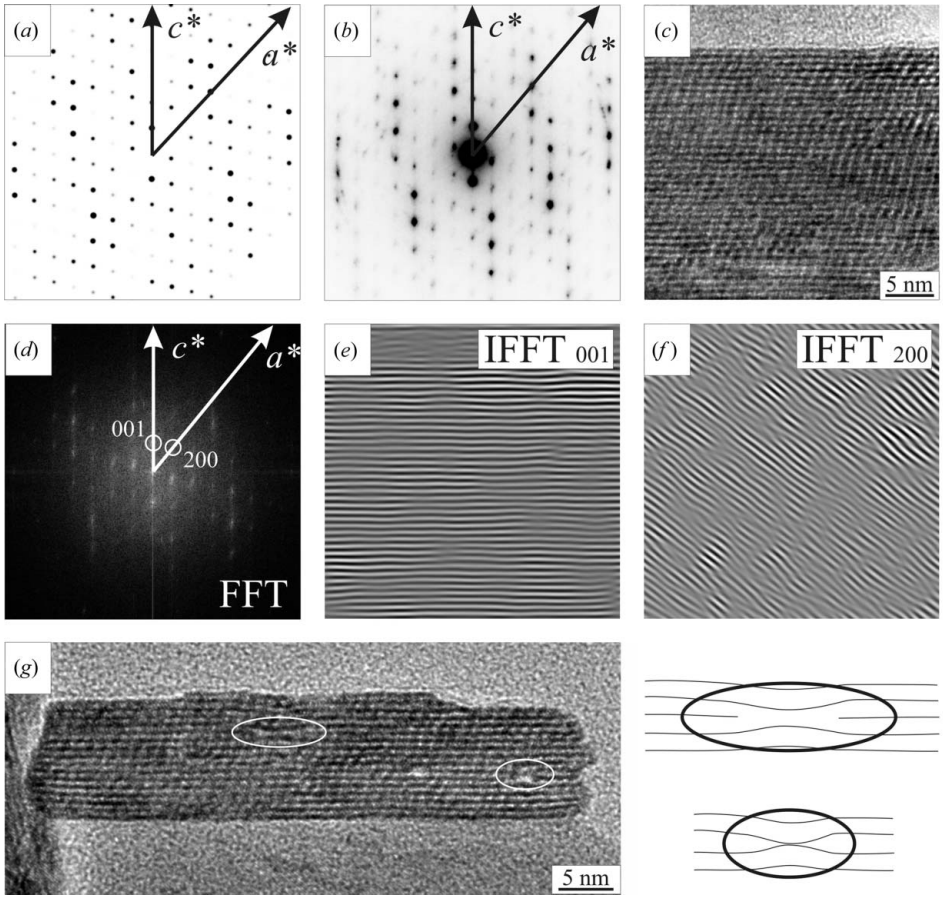

Figure 6
Zonal diffraction patterns and HRTEM micrographs of $NaTi_3O_6(OH)\cdot 2H_2O$ nanorods along the [010] direction. (*a*) Simulated zonal diffraction pattern in [010]; (*b*) experimental zonal diffraction pattern in [010] with weak diffuse scattered intensities; (*c*) HRTEM of a nanorod in the [010] projection and (*d*) its Fourier transform; (*e*)–(*f*) Fourier filtered images of (*d*) using 001 and 200 reflections; (*g*) nanorod seen in the [010] projection with two highlighted areas in the correspondence of dislocation-like defects: one defect consists of two separated edge dislocations, the other consists of two dislocations with a merged core.

from ADT data converges at compatible reliability factors (R_{wp} = 0.127, S = 1.22). Attempts to solve the structure by means of charge flipping (Coelho, 2007*b*) or direct methods implemented in *EXPO*2009 (Altomare *et al.*, 2009) were not successful due to low resolution and overlapping reflections. Therefore, XRPD data were used only for the refinement of the model obtained by ADT data. Nevertheless, due to the low quality of the XRPD data, the refinement of the O positions was problematic. After applying penalty functions (Coelho & Cheary, 1997) the Rietveld refinement (Fig. 5) converged at R_{wp} = 0.203, S = 1.45 and a feasible structural model close to that refined on ADT data could be achieved. All observed Bragg maxima were modelled by the fit.

3.6. Zonal electron diffraction and high-resolution TEM

All collected ADT tilt series showed diffuse scattered intensities along **c*** that can be more or less pronounced for different rods. This diffuse scattering indicates a pervasive disorder along the **c*** direction. In order to clarify the nature of this disorder, zonal nano electron diffraction and high-resolution TEM (HRTEM) imaging were performed.

Zonal electron diffraction patterns in [010] agree well with the simulated pattern for the proposed $NaTi_3O_6(OH)\cdot 2H_2O$ structure, both in terms of position and intensity of reflections (Figs. 6*a* and *b*). Experimental zonal patterns also confirm the presence of irregular superlattice reflections and diffuse scattering along the **c*** direction.

A high-resolution TEM image of a nanorod viewed along [010] is shown in Fig. 6(*c*). The corresponding Fourier transformation is shown in Fig. 6(*d*). The **a** axis runs parallel to the top surface of the rod, therefore the top surface of

the rod is terminated by a ⟨001⟩ sodium titanate layer. In the experimental high-resolution images irregularities are already seen in the mutual arrangement of the TiO_6 octahedra layers. Although being strictly parallel, the layers appear shifted relative to each other. This effect is more pronounced in the Fourier-filtered images. The Fourier-filtered image using the (001) reflection shows straight parallel layers with no significant perturbations (Fig. 6*e*). In contrast, the Fourier-filtered image using the (200) reflection consists of strongly distorted layers due to a shift of titania layers (Fig. 6*f*).

Besides these layer shifts HRTEMs reveal the presence of multiple edge dislocations (Fig. 6*g*). These defects are not correlated and therefore cannot be seen directly in the diffraction data. Nevertheless, they are important constituents of the bulk and therefore they are expected to significantly influence the bulk properties of the material.

4. Discussion

4.1. Comparison with related structures

Sodium titanate $NaTi_3O_6(OH)\cdot 2H_2O$ crystallizes in the monoclinic space group *C*2/*m*. The structure is built up from distorted $\{TiO_6\}$ and $\{NaO_6\}$ octahedra. The Ti—O distances range from 1.78 to 2.26, 1.88 to 2.21, and 1.73 to 2.31 Å for Ti1, Ti2 and Ti3. The individual $\{TiO_6\}$ octahedra share two common vertices and six, four or five common edges for Ti1, Ti2 and Ti3, respectively. This conformation leads to corrugated layers of condensated $\{Ti_6O_{14}\}^{4-}$ complex ions.

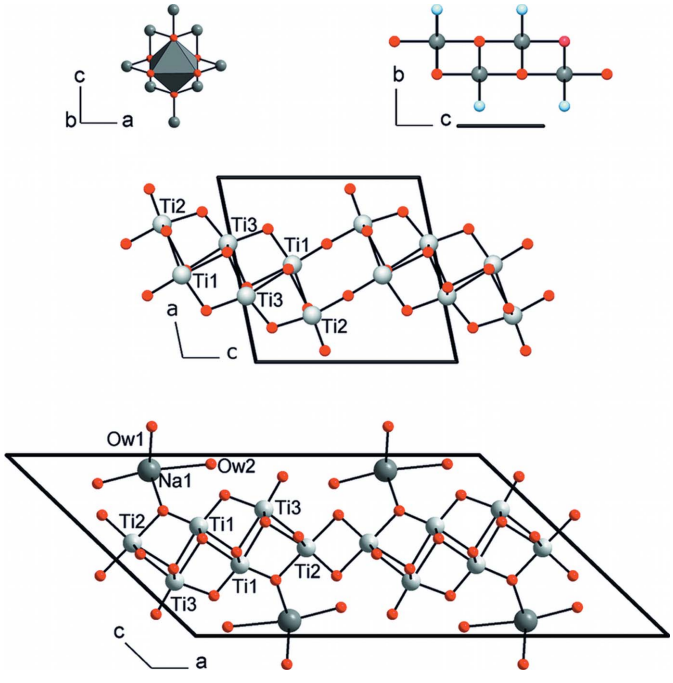

Figure 7
MO_6 octahedra (top left) and view on one layer of the lepidocrocite structure type (top right; blue: OH^-, red: O^{2-}). $\{Ti_3O_7\}^{2-}$ layers in $Na_2Ti_3O_7$ (middle) and $\{Ti_3O_6(OH)\}^-$ layers in $NaTi_3O_6(OH)\cdot 2H_2O$ (bottom).

Despite the similarity of the Ti-atom topology in $Na_2Ti_3O_7$, the connectivity of the $\{TiO_6\}$ octahedra is different. Yet, both $NaTi_3O_6(OH)\cdot 2H_2O$ and $Na_2Ti_3O_7$ may be deduced from the lepidocrocite structure (Ewing, 1935) type (Fig. 7). Starting from a hypothetical lepidocrocite-type TiO_2, both structure types can be built up by cutting and rejoining the MO_2 layers at any third translational period in the [100] direction in such a way that corrugated ribbons of edge-sharing TiO_6 octahedra are formed. While the rejoining of the resulting triple chains in $Na_2Ti_3O_7$ occurs *via* two common vertices (per translational period in [010]), in $NaTi_3O_6(OH)\cdot 2H_2O$ it occurs *via* one common edge (per translational period in [010]). In both cases this affords an additional O^{2-} ligand, resulting in negatively charged $\{Ti_3O_7\}^{2-}$ layers. Charge compensation is achieved by inserting two Na^+ cations per formula unit for $Na_2Ti_3O_7$ or one hydrated Na^+ cation and a hydroxyl group for $NaTi_3O_6(OH)\cdot 2H_2O$. Owing to the water molecules of crystallization the crystal structure of $NaTi_3O_6(OH)\cdot 2H_2O$ is more open, which is a prerequisite for its well known cation-exchange behaviour.

4.2. Disorder

The structure is built up from rigid $\{Ti_6O_{14}\}^{4-}$ layers interconnected by relatively weak Coulomb interactions with intercalated Na^+ cations and water molecules of crystallization. Therefore, an intrinsic possibility exists for shifting the $\{Ti_6O_{12}(OH)_2\}^{2-}$ layers with respect to each other in the (001) plane. The presence of such planar defects can actually produce the formation of bundles of small rods.

These shifts do not occur in the **b** direction, because the lattice parameter is too short – basically a shift along **b** is a translation transformation. In contrast, the shift of the layers along **a** is very plausible and can be chemically realised by dislocation of sodium cations and structural water molecules. This produces a deviation of the stacking vector **c**. In reciprocal space we observe a change in direction and length of vector **a***, resulting in the observed diffuse scattering along **c***.

Disorder along **a** or **b** (*i.e.* the presence of shorter blocks or fragments of $\{Ti_6O_{14}\}^{4-}$) cannot be realised as it would cause a significant change in the layer topology. In fact, there is no experimental evidence in either the three-dimensional reconstructed reciprocal space or the HRTEM imaging that suggests this kind of defect.

5. Conclusions

A new phase of sodium titanate was discovered as a structural intermediate during the synthesis of TiO_2 nanorods. Structure solution by X-ray powder diffraction was not possible as the coherently scattering crystallites are too small. Furthermore, peak broadening and overlapping strongly limited the resolution. Nevertheless, the structure was solved *ab initio* from electron diffraction data collected from single nanocrystals using the newly developed ADT module. The stability of the result was confirmed by two independent solutions from independent data sets and by Rietveld refinement based on X-

ray data. Besides the average structure a description of the correlated disorder was given based on the diffraction data and HRTEM imaging. Complete information about the structure is essential for engineering of the applications of the material.

The authors would like to thank Martin U. Schmidt (University of Frankfurt-am-Main) for extended discussions on disorder effects. The authors are grateful to the MWFZ, and Polymat (fellowship to DK) as well as to the DFG (SPP1415 and SFB625) for financial support.

References

Altomare, A., Camalli, M., Cuocci, C., Giacovazzo, C., Moliterni, A. & Rizzi, R. (2009). *J. Appl. Cryst.* **42**, 1197–1202.
Bach, U., Corr, D., Lupo, D., Pichot, F. & Ryan, M. (2002). *Adv. Mater.* **14**, 845–848.
Birkel, C. S., Mugnaioli, E., Gorelik, T., Kolb, U., Panthöfer, M. & Tremel, W. (2010). *J. Am. Chem. Soc.* **132**, 9881–9889.
Burla, M. C., Caliandro, R., Camalli, M., Carrozzini, B., Cascarano, G. L., De Caro, L., Giacovazzo, C., Polidori, G., Siliqi, D. & Spagna, R. (2007). *J. Appl. Cryst.* **40**, 609–613.
Cheary, R. W. & Coelho, A. (1992). *J. Appl. Cryst.* **25**, 109–121.
Chen, Q., Du, G. H., Zhang, S. & Peng, L.-M. (2002). *Acta Cryst.* B**58**, 587–593.
Chen, X. & Mao, S. S. (2007). *Chem. Rev.* **107**, 2891–2959.
Coelho, A. A. (2007*a*). *TOPAS-Academic*, Version 4.1. Coelho Software, Brisbane, Australia.
Coelho, A. A. (2007*b*). *Acta Cryst.* A**63**, 400–406.
Coelho, A. A. & Cheary, R. W. (1997). *Comput. Phys. Commun.* **104**, 15–22.
Denysenko, D., Grzywa, M., Tonigold, M., Streppel, B., Krkljus, I., Hirscher, M., Mugnaioli, E., Kolb, U., Hanss, J. & Volkmer, D. (2011). *Chem. Eur. J.* **17**, 1837–1848.
Ellingboe, J. L. & Runnels, J. H. (1966). *J. Chem. Eng. Data*, **11**, 323–324.
Ewing, F. J. (1935). *J. Chem. Phys.* **3**, 420–424.
Graetzel, M. (2001). *J. Sol-Gel Sci. Technol.* **22**, 7–13.
ICDD (2004). *The Powder Diffraction File* 2. International Center for Diffraction Data, Newton Square, Pennsylvania, USA.
Kasuga, T., Hiramatsu, M., Hoson, A., Sekino, T. & Niihara, K. (1998). *Langmuir*, **14**, 3160–3163.
Kim, W., Tachikawa, T., Majima, T. & Choi, W. (2009). *J. Phys. Chem. C*, **113**, 10603–10609.
Kolb, U., Gorelik, T., Kübel, C., Otten, M. T. & Hubert, D. (2007). *Ultramicroscopy*, **107**, 507–513.
Kolb, U., Gorelik, T. & Mugnaioli, E. (2009). *Mater. Res. Soc. Symp. Proc.* pp. 1184 GG01-05.
Kolb, U., Gorelik, T. E., Mugnaioli, E. & Stewart, A. (2010). *Polym. Rev.* **50**, 385–409.
Kolb, U., Gorelik, T. & Otten, M. T. (2008). *Ultramicroscopy*, **108**, 763–772.
Kolen'ko, Y. V., Kovnir, K. A., Gavrilov, A. I., Garshev, A. V., Frantti, J., Lebedev, O. I., Churagulov, B. R., Van Tendeloo, G. & Yoshimura, M. (2006). *J. Phys. Chem. B*, **110**, 4030–4038.
Lim, S. H., Luo, J., Zhong, Z., Ji, W. & Lin, J. (2005). *Inorg. Chem.* **44**, 4124–4126.
Meng, X., Wang, D., Liu, J. & Zhang, S. (2004). *Mater. Res. Bull.* **39**, 2163–2170.
Mugnaioli, E., Gorelik, T. & Kolb, U. (2009). *Ultramicroscopy*, **109**, 758–765.
Nagase, T., Ebina, T., Iwasaki, T., Hayashi, H., Onodera, Y. & Chatterjee, M. (1999). *Chem. Lett.* **9**, 911–912.
NETZSCH (2004). *Proteus-Thermal Analysis*, Version 4.3.1. NETZSCH Gerätebau, Selb, Bavaria.
O'Regan, B. & Graetzel, M. (1991). *Nature*, **353**, 737–740.
Peng, C.-W., Richard-Plouet, M., Ke, T.-Y., Lee, C.-Y., Chiu, H.-T., Marhic, C., Puzenat, E., Lemoigno, F. & Brohan, L. (2008). *Chem. Mater.* **20**, 7228–7236.
Pettersen, E. F., Goddard, T. D., Huang, C. C., Couch, G. S., Greenblatt, D. M., Meng, E. C. & Ferrin, T. E. (2004). *J. Comput. Chem.* **25**, 1605–1612.
Rozhdestvenskaya, I., Mugnaioli, E., Czank, M., Depmeier, W., Kolb, U., Reinholdt, A. & Weirich, T. (2010). *Mineral. Mag.* **74**, 159–177.
Schömer, E., Heil, U., Schlitt, S. & Kolb, U. (2009). *ADT-3D*. Institute of Computer Science, Johannes Gutenberg University, Mainz, Germany.
Sheldrick, G. M. (2008). *Acta Cryst.* A**64**, 112–122.
Strandwitz, N. C., Nonoguchi, Y., Boettcher, S. W. & Stucky, G. D. (2010). *Langmuir*, **26**, 5319–5322.
Varghese, O. K., Gong, D., Paulose, M., Ong, K. G., Dickley, E. C. & Grimes, C. A. (2003). *Adv. Mater.* **15**, 624–627.
Vincent, R. & Midgley, P. A. (1994). *Ultramicroscopy*, **53**, 271–282.
Weast, R. C. (1987–1988). *Chemical Physics*, 68th ed. Cleveland: CRC Press.
Welberry, T. R. (2004). *Diffuse X-ray Scattering and Models of Disorder*. Oxford University Press.